Multi-purpose Microwave Biosensor based on signal encoding technique and microfluidics for improved sensitivity

Mateus I. O. Souza, Achiles F. Mota, Vinícius M. Pepino, João P. Carmo, and Ben-Hur V. Borges

***Abstract*— In this paper, a microwave biosensor with unprecedented sensitivity based on encoded pulse propagation and microfluidics is theoretically investigated and experimentally demonstrated. The structure consists of a double-spiral transmission line on FR4 substrate electromagnetically coupled to a copper coiled capillary tube above it. The working principle for improved sensitivity consists of propagating an encoded sequence of short pulses (Walsh-Hadamard spreading code with variable temporal length) in a recirculating manner so that the pulses are deformed both due to dispersive and time-delay effects. Once the recirculation is finished, the energy of the code at the sensor output is calculated, providing an indicator directly related with the analyte concentration. The experimental results demonstrate the improved sensitivity of this sensor approach for the case of glucose with 2.9 mg/ml resolution. Furthermore, we demonstrate the potential of this technology as a sensor platform by investigating other chemical compounds such as isopropyl alcohol (IPA) and acetone with a sensitivity of 20% of the volume. Finally, the outstanding performance, both in terms of accuracy and sensitivity, situates the present multi-purpose approach within the state-of-the-art of microwave (bio)chemical sensors.**

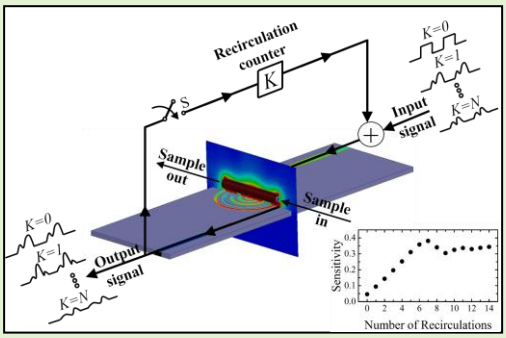

***Index Terms*—Microwave sensors; biosensors; dispersion; code division multiplexing;**

I. Introduction

In the past three decades, the advance of electronics technology in different fields of knowledge has led to a myriad of devices focused on assisting our society with its daily tasks [1]. One such field that has greatly benefited from this advance is medical sciences, with significant impact on life support equipment and monitoring devices for the treatment and diagnosis of countless diseases, such as hepatitis C [2], cancer [3], tuberculosis [4], diabetes [5], among others [6]–[8]. Currently, these monitoring devices rely basically on electrochemical [9]–[11], optical [12]–[14], acoustic [15], [16], and microwave [17], [18] technologies. Although electrochemical sensors are comparatively more accurate than their counterparts, they have a short lifetime and need constant calibration [19] due to reagent degradation [20], [21]. Optical sensors are also highly accurate but can be expensive depending on the adopted technology [22]. Acoustic sensors, in turn, are considered as an option, but large area piezoelectric films made of flexible substrates are difficult to produce, therefore discouraging investments in this field [23]. Finally, microwave sensors (despite their limited accuracy up to this date) are low-cost, easy to produce, and easily integrated with electronic systems [24]. In this sense, the scientific community has taken a growing interest in developing new microwave sensor approaches and techniques to make them as accurate as their optical and electrochemical counterparts.

One microwave sensor type that has been drawing the attention of many research groups for a long time is the glucose sensor [25], [26]. Glucose sensors are of extreme importance for the diagnose and control of diabetes, a common disease affecting over 463 million individuals around the world in 2019, according to the International Diabetes Federation [27]. Currently, the most accurate commercial blood glucose sensor is the Contour Next [28], with a 0.064 mg/ml deviation from the reference value. This electrochemical sensor based on oxidase enzyme reaction generates a small current proportional the glucose concentration when in contact with the blood sample. In most cases, each measurement takes a few minutes, preventing this technique from being used in real-time applications, particularly during surgical procedures where body fluid monitoring is of utmost importance [29], [30]. As most surgeries are classified as an invasive process, extracting samples during the procedure is not a difficult task. This sample preparation process (classified as minimally invasive) is well-suited for electromagnetic sensor technologies [31].

Most microwave sensors explore resonances whose position, magnitude, and/or shape are affected by the analyte

This work was supported in part by the Brazilian agencies CAPES, CNPq (Grants 136243/2017-7, 201880/2019-9, 303562/2017-0) and FAPESP (Grants 2013/07276-1, 2019/05248-7).

M. I. O Souza, V. M. Pepino, J. P. P. Carmo and B.-H. V. Borges are with the University of São Paulo, SP, CEP 13566-590, Brazil (e-mail: vinicius.pepino@usp.br, and benhur@sc.usp.br). A. F. da Mota is with the University of Brasilia, Brasília, DF CEP 70910-900, Brazil (email: achiles.mota@unb.br)).

composition. At resonance, the electromagnetic wave amplitude becomes very high, allowing strong interaction with any material placed above the sensor [32]. Depending on the interaction magnitude, even slight changes in the material electromagnetic parameters (permittivity ε or permeability μ) can shift the resonant frequency (f_r) [33]. This high sensitivity allows microwave sensors to measure the concentration of any substance in a sample, for instance, the glucose concentration.

The glucose concentration (C) directly correlates with the analyte ε variation [34], causing a concentration-dependent frequency shift (Δf_r) [35]. Thus, it is desirable to design sensors with wide Δf_r for small C variations (ΔC), i.e., with high sensitivity ($S = \Delta f_r/\Delta C$). The quality factor (Q) is another aspect of this sensor technology because it directly affects how accurately Δf_r is determined. To increase Q and S, and consequently the microwave sensor accuracy, many authors have resorted to resonant metamaterial cells, such as electric-LC-resonator (ELC) [36], split-ring resonators (SRRs) [25], [37], complementary SRRs (CSRRs) [35], complementary ELC-resonator (CELC) [38], interdigital capacitor (IDC) [39], among others [40], [41]. Moreover, many authors have used polydimethylsiloxane (PDMS) microchannels to place the sample inside the strong EM field produced at resonance [25], [35], [37]–[39], [42]. The resonant frequency in [34], [36]-[39] is kept constant around f_r for microchannels loaded with pure water. However, f_r shifts to lower frequencies as the glucose concentration increases (0-100 mg/ml) [25], [35], [37]–[39]. In [36], the authors have created a bandstop filter based on ELC with f_r = 3.41 GHz, achieving 20 mg/ml resolution for glucose concentrations ranging between 40 and 200 mg/ml. A resolution of 20 mg/ml has also been achieved for glucose concentrations in the range of 0-80 mg/ml in [33], and 20 to 100 mg/ml in [41]. A resolution as low as 12.5 mg/ml has been achieved with SRRs/CSRRs metamaterial cells for glucose concentration ranging between 0 and 50 mg/ml [46]. Other sensor technologies are available in [43]–[48]. It is noteworthy mentioning also the approach proposed by Cui and Wang [49] to measure the permittivity of glucose aqueous solutions. Their approach, which constitutes a different class than those listed in Table 3, benefits from the extremely narrow dynamic range allowed by interferometric techniques, rendering it extremely sensitive in the range of 0.04–18.0 mg/ml for sample volumes down to 1 nL. Nevertheless, this approach is bulky and more difficult to integrate with other systems.

In this paper, we introduce a novel multipurpose microwave (bio)sensor technology based on modulated orthogonal sequence codes (MOSC), microfluidics, and resonant coupling. To improve both sensitivity and resolution, we recirculate the encoded pulse sequence (Walsh-Hadamard spreading code) for as many times as necessary to achieve the desired performance. The pulse deformity is a function of the analyte concentration in an aqueous solution and arises due to the changes in the electric permittivity. Both theoretical and numerical (HFSS) approaches are employed to design and optimize the sensor structure/performance and to support the measured characterization data. The sensor structure consists of a double-spiral transmission line on FR4 substrate electromagnetically coupled to a copper coiled capillary tube above it. Once the recirculation is complete, we calculate the energy of the code at the sensor output, which provides a numerical indicator related to the sample concentration. The experimental results have proven the enhanced sensitivity of this sensor approach for the case of glucose with 2.9 mg/ml resolution in a range that varied from 0 to 80 mg/ml. Moreover, we demonstrate the technology potential as a sensor platform by investigating other chemical compounds such as isopropyl alcohol (IPA) and acetone with a sensitivity of 20%.

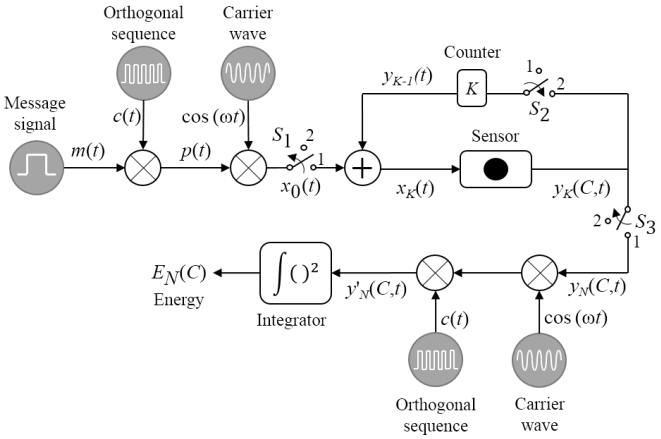

Figure 1 - Block diagram of the microwave sensor with recirculating loop.

The paper is organized as follows: Section II describes the theoretical foundation involved in the novel methodology to measure concentration of three tested substances. Section III shows the approach of the sensor. Section IV presents the biosensor design and fabrication. Section V shows the experimental characterization. Section VI describes the sensor analysis, introducing the experimental results and comparisons with previous sensor technologies. Finally, Section VII presents the conclusion and final considerations.

II. Theoretical Foundation

The block diagram of the proposed microwave sensor with signal encoding and recirculation loop is shown in Fig. 1. The architecture proposed here is general enough to be considered a platform for bio(chemical) sensor applications with adjustable sensitivity. This claim is supported by the various degrees-of-freedom offered by this technology, where all adjustable parameters affect the sensitivity and, ultimately, the sensor resolution. These parameters are the binary message $m(t)$ (type, length, and bit duration), the orthogonal sequence $c(t)$ (type of code, code length, chip duration, pulse shape), the number of signal recirculations (N), and the carrier frequency (f_0). An exhaustive combination of all these parameters is beyond the scope of this paper so, to restrict the possibilities, we have assumed the following: 1) $m(t)$ is a two-bit return-to-zero (RZ) sequence [1 0] with bit period T_b; 2) $m(t)$ is encoded with a Walsh-Hadamard (W-H) spreading sequence, similar to those used in code division multiple access techniques [50]; 3) the W-H (sequence of 1s and 0s with 50% duty cycle) sequence has a fixed length of 32 chips, where chip is the time interval of length T_c corresponding to one symbol of the spreading sequence; 4) the bit duration $T_b = T_c \times 32$. The sequence length of 32 chips has been chosen due to the sampling rate limitation of our arbitrary wave generator (AWG).

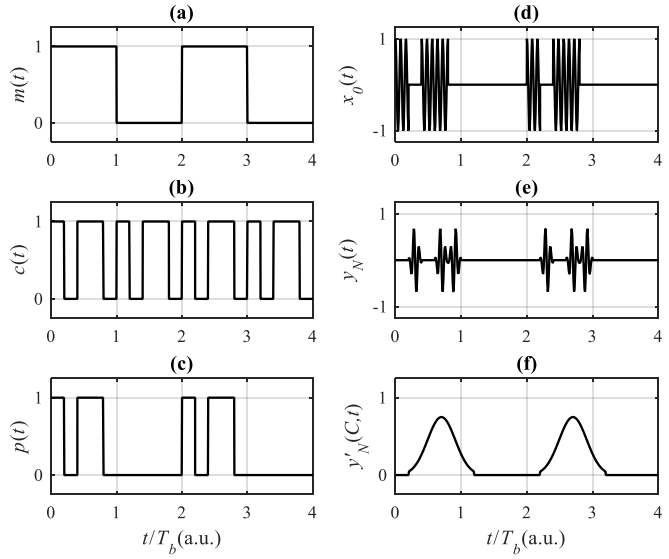

Figure 2 - Encoding and modulating processes, where (a) is the code message, (b) the orthogonal sequence, (c) the encoded message, (d) the modulated encoded message, (e) the encoded message after propagating through the sample, and (f) the message recovered after propagating through the sample.

Thus, from Fig. 1, after multiplying $m(t)$ by the W-H spreading code $c(t)$ we obtain a signal $p(t) = m(t)c(t)$, where each bit period T_b now becomes divided into chips with duration T_c. Next, $p(t)$ is multiplied by the carrier frequency as follows,

$$x_0(t) = p(t)\cos(\omega t), \tag{1}$$

where ω (=$2\pi f_0$) is the angular frequency. Chips are usually square pulses in CDMA technology. However, here we explore three different chip pulse shapes, namely, Gaussian, triangular, and trapezoidal (where the trapezoidal is the best representation for square pulses in practical setups). Figures 2(a)-(f) show the signal profile of $m(t)$, $c(t)$, $p(t)$, $x_0(t)$, $y_N(C,t)$ and $y'_N(C,t)$, respectively. $y_N(C,t)$ represents the concentration-dependent signal output, while y'_N is their demodulated and decoded form. Figures 3 (a)-(c) show the Gaussian, triangular, and trapezoidal pulses as function of time, respectively, and their respective MOSC spectra (d)-(f). The Gaussian pulse has a full width at half maximum of $T_c/8$, so that approximately 100% of the pulse energy is within the chip time slot. We assume rise and fall times of $T_c/2$ for the triangular pulses, and $T_c/4$ for the trapezoidal pulses.

Using these chip pulse shapes, the propagation sequence, $x_0(t)$, is allowed to recirculate through the biosensor as many times as the desired accuracy requires. A counter K (K = 0, ..., N) is included in the feedback loop to count the number of circulations. During the first circulation (K = 0), switches S_1 and S_3 are closed and S_2 open. However, switch S_1 remains open during all recirculation cycles (K > 0) with the signal input updated as follows,

$$x_K = y_{(K-1)}. \tag{2}$$

After finishing the recirculations, the propagated codes are synchronously decoded at the receiver end. The signals propagated through pure water are used as reference to align the other samples with their respective base signal for the decoding stage, keeping the delay between them. Since ε and tan δ are a function of the sample concentration, the delay and attenuation

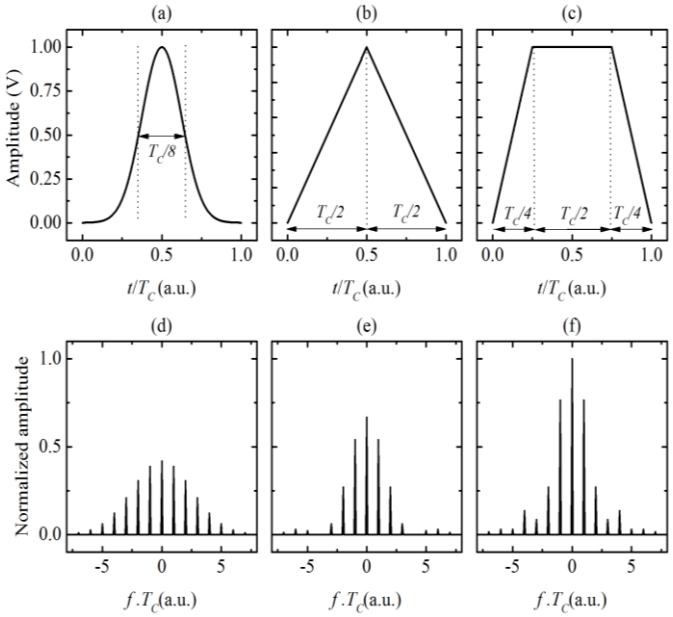

Figure 3 - (a) Gaussian, (b) triangular, and (c) trapezoidal pulse shapes for the chip pulse used on the MOSC. (d)-(f) are their respective MOSC frequency representation.

suffered by every propagating signal are automatically incorporated into the decoding process. In order to recover the information transmitted through the sensor, the signal $y_N(C,t)$ must be demodulated and decoded. As follow,

$$y'_N(C,t) = y_N(C,t)c(t)\cos(\omega t). \tag{3}$$

Finally, we calculate the energy by integrating $y'_N(C,t)$ as follows,

$$E_N(C) = \int_0^T \left[y'_N(C,t)\right]^2 \mathrm{d}t, \tag{4}$$

where $E_N(C)$ is the signal energy after N recirculations, and T is the signal period. Next, we discuss two different schemes for this sensor approach.

It is important to emphasize that the recirculation loop requires the signal to be pulsed. The choice of pulsed propagation signals are as follows: (*i*) single pulse, (*ii*) binary sequence, and (*iii*) orthogonal code sequences (Walsh-Hadamard, in our case), with the last two of arbitrary length. With a (*i*) single pulse signal, it is virtually impossible to resolve the energy variation as function of the concentration, particularly for glucose because the sample permittivity varies only slightly over the range of interest. This occurs because both the dispersion and time delay after propagation are insignificant compared to the bit length T_b, as will become clear as the text progresses. The (*ii*) binary sequence, unfortunately, suffers from the same problems experienced in (*i*). But it is worth emphasizing at this point that, regardless the choice of signal (*i*, *ii*, or *iii*), the bit length T_b must always be the same. In contrast, the chip duration T_c changes according to $T_c = T_b/32$, with 32 as the number of chips defined here based on our hardware limitation. Thus, T_b is much longer than any variation it might suffer due to chromatic dispersion and time delay, rendering it essentially constant in terms of energy content for different analyte concentration. Moreover, the minuscule energy variation of each pulse makes this type of sequence more

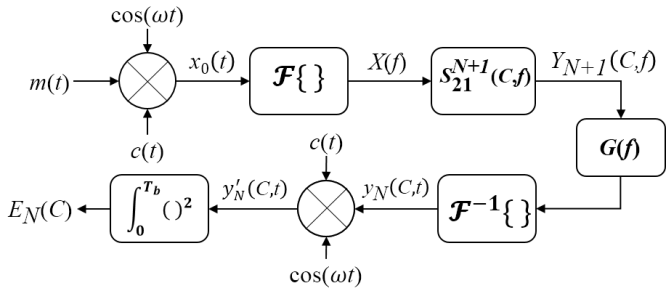

Figure 4 - Block diagram of the sensor operating principle of scheme (A) relating the substance concentration with the energy at the sensor output via Fourier Transform in frequency domain.

prone to post-processing errors and detection ambiguity issues. Finally, we are left with the orthogonal code sequences, where a binary sequence is encoded according to a predefined signature. What makes these sequences attractive to this approach is that the decoding process is extremely sensitive to the propagation channel non-idealities (this is a classical issue in CDMA telecommunication systems). Therefore, the longer the encoded sequence received, the higher the impact of the signal degradation on the correlation process and, consequently, the higher the sensor sensitivity. The choice for W-H codes is because this sequence completely satisfies all requirements and limitations for experimental implementation with our current infrastructure. Next, we discuss two different schemes for this sensor approach.

III. Approach

We realize this sensor approach by means of two different schemes. The first scheme (A) consists in experimentally extracting the S-parameters and, through a mathematical algorithm (via sensor transfer function), we obtain the analyte concentration. This concept is straightforward to implement because it does not require additional hardware (only a vector network analyzer (VNA) and a computer). Moreover, we use this scheme to optimize all sensor parameters, i.e., f_0, T_c, pulse format and N, to achieve the highest possible sensitivity. These optimized parameters are used in the second scheme (B) which is essentially a hardware implementation of the first. This second approach is used here as proof-of-concept for future integration of the sensor.

Differently from conventional microwave sensors (based on continuous wave) [25], [35]–[42], here we explore the analyte frequency dependent permittivity (chromatic dispersion) and its impact on the pulse shape at the end of each propagation cycle (recirculation). Usually, the analyte concentration variation is not strong enough to be sensed at the device output, such as in glucose sensors. Therefore, the more the pulse sequence interacts with the analyte (via recirculation), the better. In this sense, the number of recirculations is limited by the combined loss of both the sensor structure and the analyte, and the detection sensitivity.

An important issue regarding the approach in Fig. 1 is the chip bandwidth. Large bandwidths, although desirable from the chromatic dispersion point of view, may cause the pulse frequency components to disperse into S_{21} regions whose frequency dependence is not well-behaved. When that occurs, the S_{21} curves for different analyte concentrations follow an

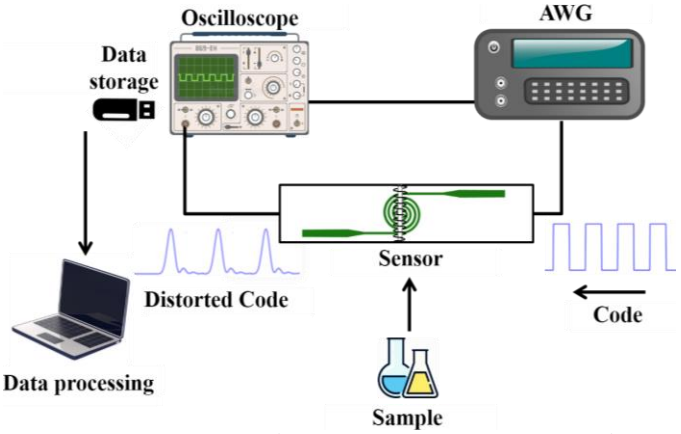

Figure 5 - Schematic diagram for the experimental implementation of scheme (B), where the measured energy is compared with that of scheme (A) for validation purpose.

irregular behavior difficult to resolve during signal processing. To solve this issue, we recommend shorter chip bandwidths and well-behaved S_{21} curves, i.e., curves unambiguously separated, sequentially following the sample concentration within a given bandwidth.

A. Transfer-function scheme

This scheme consists in extracting the biosensor transmission S-parameters for different concentrations, $S_{21}(C,f)$, which is experimentally accomplished with a VNA. The block diagram of this scheme is schematically shown in Fig. 4. Note that $x(t)$ is generated according to Fig. 1 and Eq. (1). However, to use the scattering parameters, we need to Fourier transform (FT) $x_K(t)$. Note that when $K = 0$ at the sensor input (i.e., no propagation and recirculation through the sensor), $X_0(f)$ depends only on the frequency (it depends on both frequency and concentration for $K > 0$). Thus, for $K = 0$,

$$X_0(f) = \int_{-\infty}^{\infty} x_0(t) e^{-j2\pi ft} dt \cdot \tag{5}$$

Next, we numerically calculate the output signal FT after N propagations through the sensor, $Y_N(C,f)$, as follows,

$$Y_N(C,f) = X_0(f)\left[S_{21}(C,f)\right]^{N+1}. \tag{6}$$

Note that the frequency response of the output signal must be obtained for each concentration. Thus, the biosensor response in time domain, $y_N(C,t)$, is calculated by inverse Fourier transforming $Y_N(C,f)$ after passing through a Gaussian filter, $G(f)$, as follows,

$$y_N(C,t) = \frac{1}{2\pi}\int_{-\infty}^{\infty} Y_N(C,f) G(f) e^{j2\pi ft} df. \tag{7}$$

The Gaussian filter is centered at the operating frequency of each case, with a 20 MHz bandwidth. The demodulated and

Table 1 - Sensor geometric parameters in (mm) relative to Fig. 6.

l_1	l_2	l_t	a	b	A	B	H_c
3.1	3.3	30	20	1	96	32.7	4.3

H_d	D_w	L_c	D_{in}	D_{out}	D_{Cin}	D_{Cout}
1.6	0.6	23.8	2.3	3.5	1	1.5

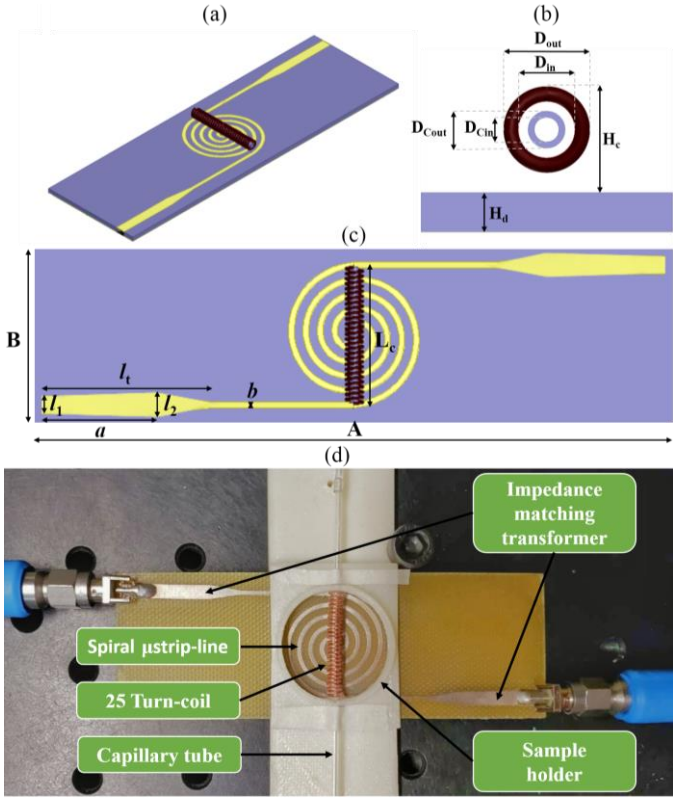

Figure 6 - Proposed biosensor: (a) 3D view of the biosensor (ground plane not shown), (b) capillary and coil dimensions and (c) line dimens ions. (d) is the fabricated sensor.

decoded signal $y'_N(C,t)$ is calculated by substituting $y_N(C,t)$ back into (3). Finally, the signal energy $E_N(C)$ is obtained with the help of (4).

B. Hardware implementation scheme

The optimized MOSC parameters from the first scheme are now used in the hardware implementation schematically shown in Fig. 5. Here, the signal is analyzed in time domain, and the energy $E_N(C)$ is calculated after the signal has physically (re)circulated through the biosensor. The signal $x_K(t)$ is generated with an arbitrary wave generator (AWG), which is also responsible for reinjecting the signals to be recirculated back into the sensor input.

The signal (re)circulation circuit operates as follows. First, the signal $x_0(t)$ is injected into the sensor input by the AWG. Assuming no recirculation at the moment, after propagating through the sensor, the output signal $y_0(C,t)$ is acquired by a high-frequency oscilloscope (HFO) and then post-processed with a Matlab code. In the Matlab environment, we calculate $y'_0(C,t)$ and $E_0(C)$ from (3) and (4), respectively, from which we estimate the sample concentration. If recirculation is required, the signal $y_0(C,t)$ from the HFO is loaded with a flash drive back into the AWG and renormalized to produce the next input signal $x_1(C,t)$, which is then reinjected into the biosensor to produce $y_1(C,t)$. This procedure is repeated N times, until the desired number of recirculations is reached. This process is time consuming but will be fully automated in future implementations of this sensor. When all $y_N(C,t)$ are measured, the data is post-processed in Matlab to obtain $y'_N(C,t)$ and $E_N(C)$ from (3) and (4), respectively. Finally, the sample concentration

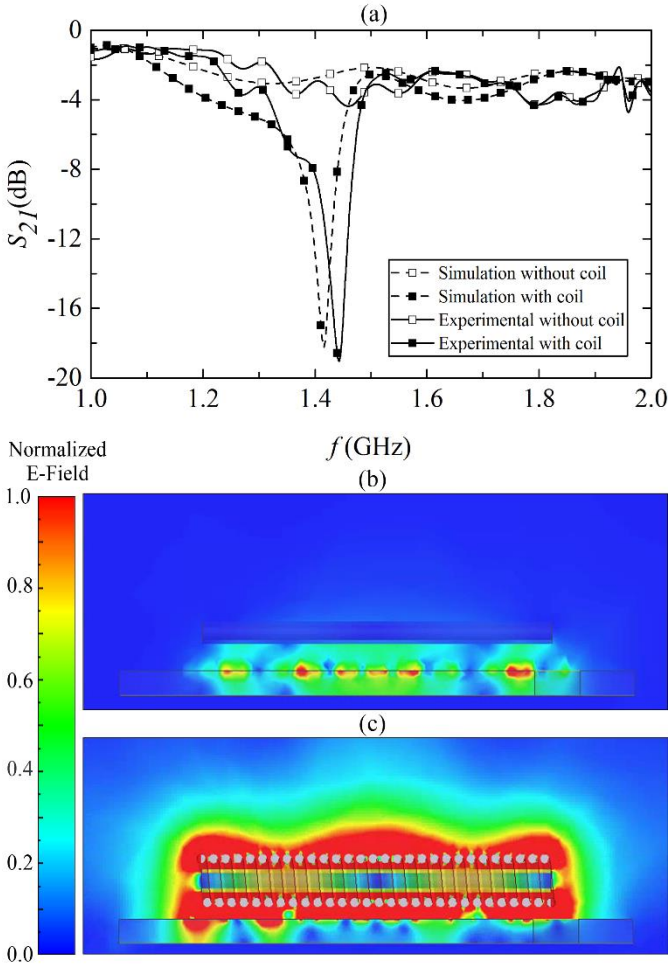

Figure 7 – Sensor behavior under different operating conditions. (a) Measured (squares, solid lines) and simulated (squares, dashed lines) frequency response without and with the coil. Electric field over the microstrip line (b) without and (c) with the coil.

is obtained from $E_N(C)$. In the next section, we discuss the design of the microwave biosensor.

IV. BIOSENSOR DESIGN AND FABRICATION

The proposed biosensor is a two-turn spiral microstrip-line built on top of an FR4 substrate (ε_r = 4.3 - 0.05j) with a ground plane, as depicted in Fig. 6(a). We use an impedance matching transformer at the spiral input and output ports to avoid undesired reflections. Figures 6(b) and (c) show the sensor geometric parameters, while (d) shows its hardware implementation. We have added a thin layer of silver nitrate over the copper tracks to avoid oxidation and, consequently, signal degradation during the measurements, and also to extend the sensor lifetime. A 25-turn copper coiled capillary tube (through which the analyte is injected) placed above the microstrip spiral completes the sensor architecture. Note that the coil is not physically connected with the microstrip and the resonance is a result of the strong field interaction between the cooper coil and the microstrip spirals. We simulate this structure with the commercial finite element software HFSS 15.0 from Ansys [51]. The copper coil is resonantly coupled with the microstrip spiral, as shown in Fig. 7 (a) for water filled capillary. The S_{21} behavior for the non-coiled capillary (empty squares), although somewhat wavy, is still adequate for the

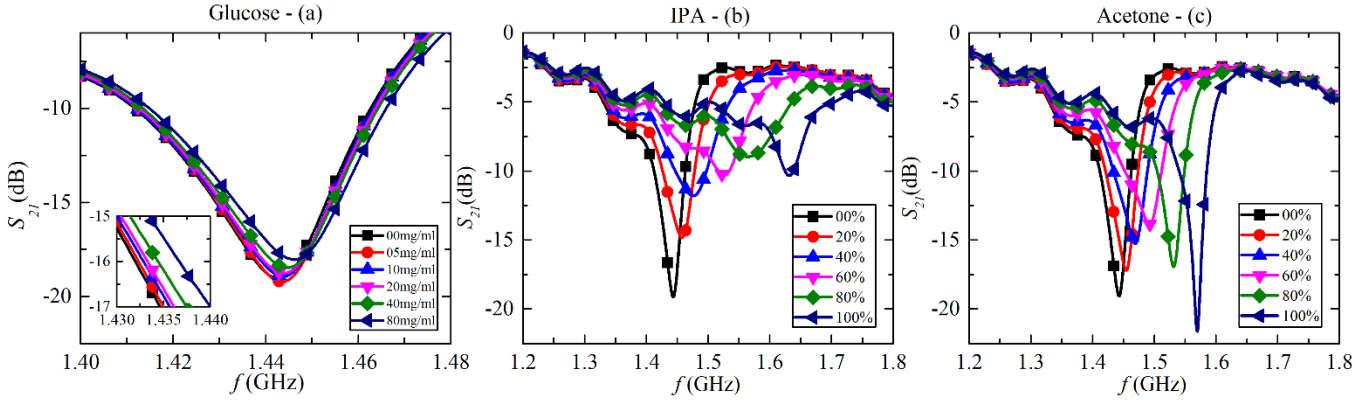

Figure 8 - Frequency response in magnitude for the three substances: (a) glucose, (b) IPA and (c) acetone for different concentrations.

purpose of pulse dispersion management, as discussed in the beginning of section III.

The electric field distribution surrounding the non-coiled capillary, shown in an orthogonal plane with respect to the coil longitudinal axis in Fig. 7 (b), indicates that the current along the microstrip induces a weak electromagnetic field above the sensor and, consequently, a weak field interaction with the analyte. However, when the coil is present (solid squares), as observed from the simulation (dashed lines) and experimental (solid lines) curves, we obtain a strong resonance around 1.43 GHz, adopted here as the sensor operating frequency. Figure 7 (c) shows the intensification of the electric field surrounding the coiled capillary at resonance. At this condition, the field interaction with the analyte increases substantially, leading to higher sensitivity and resolution. Table 1 lists the optimized sensor geometrical parameters used during simulation and fabrication.

V. Experimental Characterization

Before we proceed with the experimental characterization, it is worthwhile explaining why we have chosen glucose, IPA, and acetone as our test analytes. These substances allow us to stress the sensor performance via their concentration-dependent permittivity, ranging from slight variation (glucose) to substantial variation (acetone and IPA). To better understand the sensor characterization, we have organized this section as follows. First, we explain how to obtain the frequency response for these substances. Next, we obtain their concentration-dependent frequency responses and use them as transfer-functions in scheme A, which allows us to choose the best operating point for each substance. We use these points to prove experimentally the concepts behind our approach. To prepare the glucose sample, we use serial dilution where a highly concentrated glucose sample (80 mg/ml) is successively diluted in pure water to obtain the concentrations of 40, 20, 10 and 5 mg/ml. The IPA and acetone samples, in contrast, are diluted in water with different ratios, 1:1 (100%), 4:5 (80%), 3:5 (60%), 2:5 (40%), 1:5 (20%), 0:1 (0%). The lowest concentration was chosen based on the accuracy we can achieve with our sample preparation methodology. Nonetheless, it is important to emphasize that smaller concentrations can also be resolved with our sensor technology, because the sensitivity can be controlled by changing the size of the encoded sequence. We use a syringe to insert each sample into the capillary tube, discarding the sample after the measurement is complete. The capillary tube cleansing requires only 5 ml of pure water between each measurement cycle. The frequency response of each sample is then measured with the VNA (Rohde&Schwarz ZVA 40) to obtain $S_{21}(f,C)$.

Figure 8 shows the frequency response $S_{21}(f,C)$, with the concentration as a parameter, for (a) glucose, (b) IPA, and (c) acetone (all in aqueous solution). We used 5001 points for each substance, with an output power of 0 dBm and intermediate frequency bandwidth of 25 kHz. Note in (a) that the glucose concentration range is too low to produce a significant variation in S_{21} (due to the small change in the analyte permittivity in the considered concentration range [34]). The inset of this figure shows that the curves are sequentially arranged from left to right from low to high glucose concentrations. This arrangement comes from the well-behaved S_{21} responses that help to resolve the subtle glucose variations during signal post-processing. This discussion is also valid for the IPA and acetone responses, shown in (b) and (c).

After extracting the frequency responses $S_{21}(f,C)$, we use them in scheme A to optimize T_c, f_0, N, and the pulse shape. It is worth noticing that the optimum T_c, f_0, N are those that produce the highest variation of $E_N(C)$ for different concentrations, especially for slight variations of C. In this sense, we define the figure-of-merit

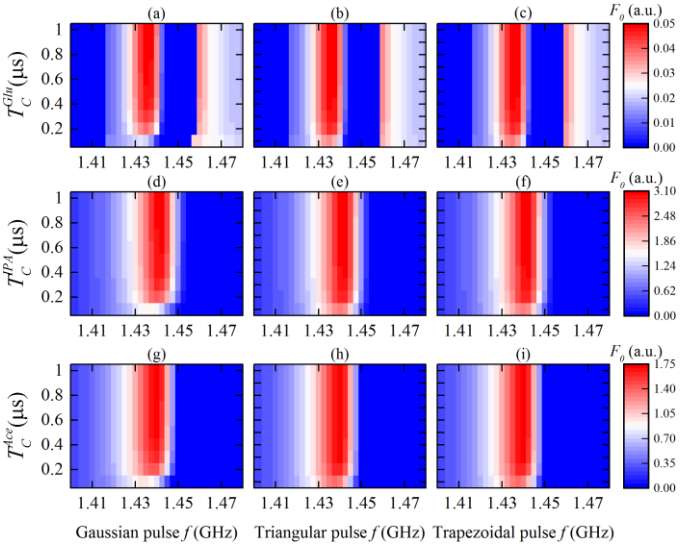

Figure 9 - Simulated F_0 maps (no recirculation) as function of the chip period Tc, operating frequency f, and pulse shape. First, second, and third columns represent gaussian, triangular, and trapezoidal pulse shapes, respectively. First, second, and third rows represent Glucose, IPA and acetone, respectively.

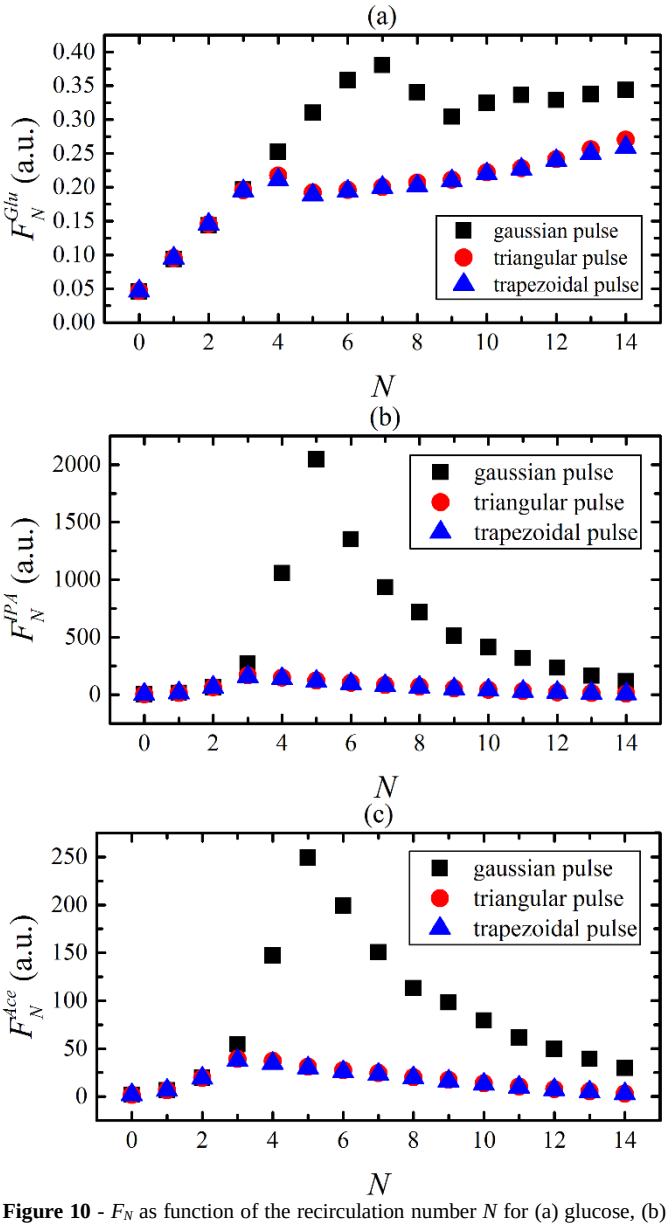

Figure 10 - F_N as function of the recirculation number N for (a) glucose, (b) IPA, and (c) acetone. The pulse shape is taken as a parameter.

$$F_N = \frac{E_N(C_1) - E_N(C_2)}{E_N(C_1)}, \tag{7}$$

which gives the simulated normalized energy difference between the two lowest concentrations, where C_1 is for pure water and C_2 is 5 mg/ml for glucose (C_2 is 20% for IPA and acetone). First, we set $N = 0$ to obtain the T_c and f_0 values that return the highest F_0 for a single propagation. Then, we use these values to perform multiple recirculations (N) and to obtain F_N for the three pulse shapes. The optimum set of parameters (T_c, f_0, N, and pulse shape) is the one that produces the highest F_N.

Figure 9 shows the simulated F_0 for scheme A with 1.4 GHz < f_0 < 1.48 GHz and 0.1 μs < T_c < 1 μs for glucose (first row, (a-c)), IPA (second row (d-f)), and acetone (third row (g-i)). For the sake of visual clarity, F_0 is set to zero at the T_c and f_0 points where S_{21} is ill-behaved. The F_0 maps show only the regions where the S_{21} curves are well-behaved, as previously discussed. The columns in this figure represents F_0 calculated for Gaussian (first column (a,d,g)), triangular (second column (b,e,h)), and trapezoidal (third column (c,f,i)) pulse shapes. Note that the pulse shape has little to no influence on F_0 for any of the substances. Consequently, the optimum f_0 and T_c are identical regardless of the pulse shape. The optimum f_0 is 1.435 GHz for glucose and 1.44 GHz for IPA and acetone. At these points, the variation between $S_{21}(f,C_1)$ and $S_{21}(f,C_2)$ is maximum, as seen in Figs. 8(a-c), and F_0 increases with T_c until it saturates at approximately T_c = 800 ns for the three substances. This behavior occurs because, as T_c increases, the pulse bandwidth narrows, concentrating the code energy in the frequency range where the difference between $S_{21}(f,C_1)$ and $S_{21}(f,C_2)$ is higher, therefore increasing F_0. However, at T_c = 800 ns, the energy is already concentrated in a narrow spectrum, and increasing T_c further does not significantly contribute to increasing F_0. In addition, longer T_c values also mean longer periods for $x_K(t)$ and $y_K(t)$ and, consequently, longer recirculating and post-processing times. The saturation of F_0 for T_c > 800 ns shown in Fig. 9 indicates that there is a ceiling for the maximum pulse width to maximize sensitivity. Therefore, we use the smallest pulse bandwidth that still produces a high F_0 value. Thus, assuming T_c = 800 ns (resulting in F_0 = 0.05, 3.1, and 1.75 for glucose, IPA, and acetone, respectively) is a good compromise between operation time and F_0.

Once the optimization of T_c and f_0 is complete (note that we are still in scheme A), the next step is to decide on both the pulse shape and recirculation N. Figure 10 shows the normalized energy difference F_N as function of N for Gaussian (squares), triangular (circles), and trapezoidal (triangles) pulse shapes for glucose (a), IPA (b), and acetone (c) samples. The pulse shape does not affect F_N significantly for $N \leq 3$. However, for $N > 3$, the Gaussian pulse produces a marked enhancement in F_N when compared to the triangular and trapezoidal pulse shapes. The narrow bandwidth of the Gaussian pulse profile favors the S_{21} curves to be arranged sequentially, according to the sample concentration. The optimum recirculation number for glucose, IPA, and acetone is N = 7 (F_7 = 0.38), 5 (F_5 = 2045), and 5 (F_5 = 208), respectively. The curve saturation observed at these points occurs due to the sensor stopband behavior. The recirculation number provides a metric of how strongly the sensor sensitivity is affected with the increase of F_N, that is, by approximately 8, 680, and 120 times for glucose, IPA, and acetone samples, respectively when compared to F_0. Table 2 summarizes the optimum parameter values for the three substances.

VI. Sensor Analysis

The optimum pulse shape and parameters for the three substances are now used in the implementation of scheme B. Figures 11(a)-(c) show the energy (normalized to pure water) for glucose (E_7^{Glu}) (a), IPA (E_5^{IPA}) (b) and acetone (E_5^{Ace}) (c) as function of the concentration for schemes A (empty circles) and B (black squares). The energy in Fig. 11(a) is fitted by a first order polynomial given by,

$$\log_{10}(E_7^{Glu}) = 16.21\times10^{-3}C + 4,67\times10^{-3}. \tag{8}$$

Each measurement is carried out 5 times, and the average error is 0.0468 a.u. (error in $\log_{10}$ base). The sensor sensitivity is

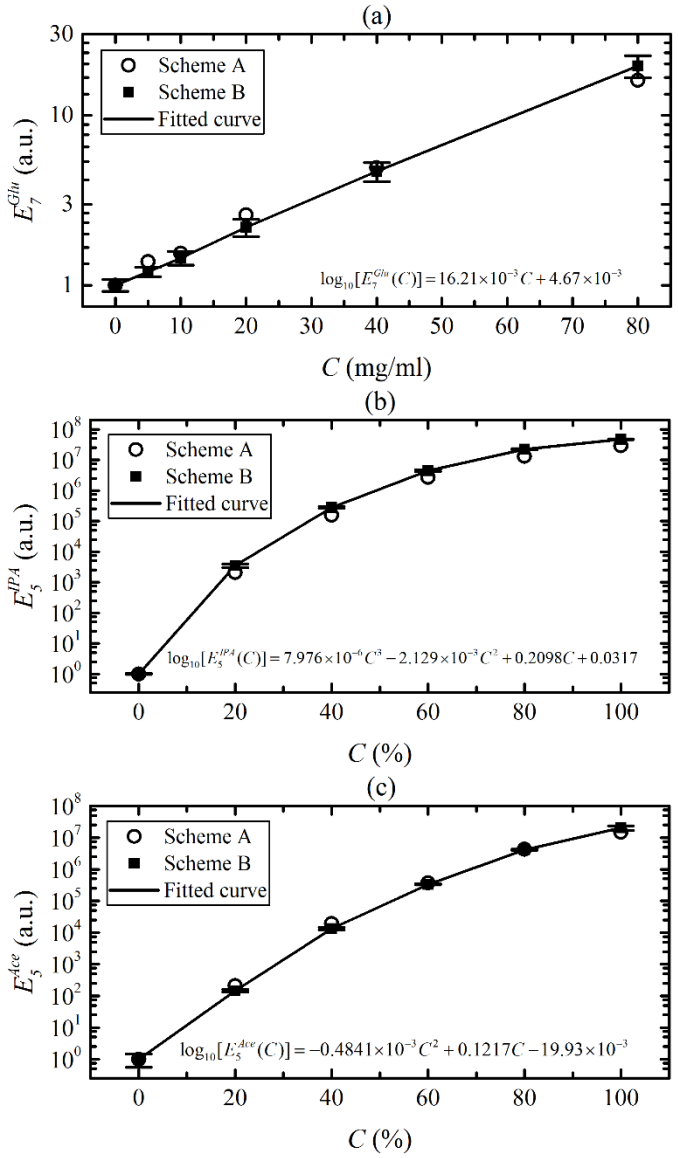

Figure 11 - Normalized energy as function of the concentration for (a) glucose (in mg/ml), (b) IPA (% volume), and (c) acetone (% volume).

defined as the ratio between the variation of $\log_{10}(E_{glu})$ to that of C_{glu} [48],

$$S_{glu} = \frac{\Delta \log_{10}\left(E_{glu}\right)}{\Delta C_{glu}} = 0.0161 \quad (\text{mg/ml})^{-1}. \tag{9}$$

Thus, we can calculate the sensor resolution by dividing the uncertainty (0.0468 a.u.) by the sensitivity S_{glu} [48], resulting in 2.9 mg/ml. The normalized energy for IPA and acetone, both as function of the concentration (%), is shown in Figs. 11(b) and (c), respectively. These curves are best fitted by a third and second order polynomial, respectively, as follows,

$$\log_{10}\left(E_{IPA}\right) = 7.976\times10^{-6}C_{IPA}^3 + 0.0021C_{IPA}^2 + 0.21C_{IPA} + 0.0317, \tag{10}$$

$$\log_{10}\left(E_{Ace}\right) = 4.841\times10^{-4}C_{Ace}^2 + 0.1217C_{Ace} - 0.02. \tag{11}$$

The average energy error for IPA and acetone are 0.03 a.u. and 0.06 a.u., respectively. The calculated sensitivity for these substances is,

Table 2 - Defined parameters for the MOSC signal.

Substance	f_0 (GHz)	T_c (ns)	F_0	N	F_N	Chip format
Glucose	1.435	800	0.05	7	0.38	Gaussian
IPA	1.44	800	3.00	5	2045	Gaussian
Acetone	1.44	800	1.73	5	208	Gaussian

$$S_{IPA} = \frac{\Delta \log_{10}(E_{IPA})}{\Delta C_{IPA\%}} = \frac{7.767(\text{a.u.})}{100(\%)} = 0.07767\,(a.u.)/\%, \tag{12}$$

$$S_{Ace} = \frac{\Delta \log_{10}(E_{Ace})}{\Delta C_{Ace\%}} = \frac{7.31(\text{a.u.})}{100(\%)} = 0.0731(a.u.)/\%. \tag{13}$$

The IPA and acetone sensor resolutions are then 0.39% and 0.82%, respectively.

Next, we compare the performance of our sensors with those available in the literature [44-57]. It is worth pointing out that these works use a different technique to measure the glucose concentration. The most used parameter is the shift in the transmission parameters ΔS_{21}, but there are other approaches such as ΔQ [46], ΔE (this work), among others [39], [43], [45], [52], [53]. Therefore, to make a fair comparison between our approach and those from the literature, we define here the normalized sensitivity,

$$S_N = \frac{\Delta X / X_{\max}}{\Delta C} \cdot 100, \tag{14}$$

where X is the parameter used to infer the analyte concentration and ΔC is the concentration range (in mg/ml or %). In our case, X is the normalized energy E_N. For instance, comparing the non-recirculation case with the best-case scenario for glucose (N = 7), we find that the normalized sensitivity increases from 0.39% $(\text{mg/ml})^{-1}$ to 1.19% $(\text{mg/ml})^{-1}$. Therefore, the recirculation loop introduced here increases the glucose sensor sensitivity by 205%. Next, we use the same procedure for the other two substances. For IPA, we obtain a normalized sensitivity of 0.95% with N = 0, reaching 1% for N = 5. A similar result has been obtained for acetone, with a normalized sensitivity of 0.94% with N = 0, reaching 1% with N = 5. Therefore, a sensitivity increase of 5% and 6% for IPA and acetone, respectively, is obtained with the present approach. Table 3 lists a comparison between different microwave glucose and IPA sensors currently available in the literature and our approach (no acetone sensor approach is currently available). We have selected the best relative sensitivity (S_N) from the selected publications, and the cases where the sensitivities depend on the ΔS_{21} parameter the normalization is made in linear scale. Note that the sensor proposed here has both the highest sensitivity (1.19% $(\text{mg/ml})^{-1}$) and resolution (2.9 mg/ml) in the 0-80 mg/ml concentration range for the glucose. Our approach also exhibits the highest sensitivity for IPA when compared to [52]–[55]. Moreover, our sensor operates at a lower frequency (1.4 GHz) compared to other approaches and utilizes a cheap substrate (FR4). The only drawback is the larger sample volume when compared to other sensors.

VII. Conclusion

In this paper, we have implemented, both theoretically and experimentally, a microwave biosensor based on encoded pulse propagation and microfluidics. The structure consisted of a

Table 3 - Comparison of recently published microwave glucose and IPA sensor results, listing their respective operating frequency, resolution, concentration range, and normalized sensitivity.

	Structure	f_r (GHz)	Measured parameter	Resolution (mg/ml)	Range (mg/ml)	Sample Vol. (µL)	Substrate	S_N (% ml/mg)	Year	Ref.
Glucose	MEMS	15.24	$\Delta f_r(S_{11})$	57.3	0-347.8	-	Silicon	0.2875*	2009	[43]
	CELC	1.5	$\Delta f_r(S_{21})$	20	0-100	-	RO6002	0.9616*	2015	[38]
	OSRR	5.24	ΔS_{21}	10	0-400	-	RO3003	0.2375*	2015	[44]
	IDC	7.5	ΔS_{21}	0.31	0.3-80	-	SU-8	0.172*	2016	[48]
	SRR	2.46	ΔS_{21}	40	40-200	20	DiClad880	0.1890*	2017	[47]
	CSRR	5.41	$\Delta f_r(S_{21})$	20	0-80	100	RT 5880	0.1455*	2018	[35]
	ELC	3.41	ΔS_{21}	20	40-200	20	DiClad 880	0.0759*	2018	[36]
	IDT	3.9/7.95	$\Delta f_r(S_{11})/\Delta f_r(S_{11})$	110	0-1000	15	FR4	0.1*	2018	[39]
	ENG	2.07	$\Delta f_r(S_{21})$	20	0-100	-	FR4	1.004*	2018	[41]
	SRR	2	$\Delta f_r/\Delta A$	10	10-150	-	Rogers5880	0.1489*	2018	[45]
	Reson.	2/5/7	$\Delta Q(S_{21})$	12.5	0-100	2-25	Tac. TLX-8	1*	2019	[46]
	SRR	4.18	ΔS_{21}	12.5	0-50	-	RT6006	0.31*	2019	[37]
	This work	**1.44**	**ΔE**	**2.9**	**0-80**	**235**	**FR4**	**1.1860**	**2020**	**-**

	Structure	f_r (GHz)	Measured parameter	Resolution (%)	Range (%)	Sample Vol. (µL)	Substrate	S_N (%)	Year	Ref.
IPA	THZ-FDS	625	ΔA	20	0-91	20	Quartz	0.8169*	2013	[52]
	Reson.	19.2	$\Delta S_{21}/\Delta f_r(S_{21})$	20	0-80	$45x10^{-6}$	SU-8	0.8845*	2019	[54]
	IDE	3	$\Delta S_{11}/\Delta f_r$	20	0-100	1	FR4	0.3506*	2019	[53]
	IDC	0.03	ΔS_{21}	5	0-100	-	Glass	0.8876*	2019	[55]
	This work	**1.44**	**ΔE**	**0.39**	**0-100**	**235**	**FR4**	**1**	**2020**	**-**

* Values calculated by us.
- Not informed by the authors.

double-spiral transmission line on FR4 substrate electromagnetically coupled to a copper coiled capillary tube above it. The working principle for improved sensor performance was the propagation of an encoded sequence of short pulses (32-chip Walsh-Hadamard spreading code with variable temporal length) in a recirculating loop to enhance the sensitivity and accuracy. The signal energy is a function of the analyte concentration in aqueous solution and arises due to changes in the electric permittivity. The encoding sequence recirculates through the structure as many times as necessary both to achieve the desired sensitivity and to reduce the error between successive measurements. Once the recirculation is finished, the energy of the code at the sensor output is calculated, providing a causally related response to the analyte concentration.

The experimental results proved the improved sensitivity of this sensor approach for the case of glucose with 2.9 mg/ml resolution. Furthermore, we have also demonstrated the potential of this technology as a sensor platform by investigating other chemical compounds such as isopropyl alcohol (IPA) and acetone, both with a sensitivity of 20% of the volume. The outstanding performance, both in terms of accuracy and sensitivity, situates the present multi-purpose approach within the state-of-the-art of microwave (bio)chemical sensors. Finally, another positive aspect of using orthogonal sequences, not explored in this paper, is the use of multiple encoded sequences simultaneously to probe additional responses of a given sample. In fact, this is the next step in the evolution of our current approach. The use of multiple sequences is related to two fundamental properties of code formation, namely, orthogonality and cardinality, that potentially paves the way to improving current sensor technologies and exploring new ones.

REFERENCES

[1] M. R. Neuman *et al.*, "Advances in medical devices and medical electronics," *Proc. IEEE*, vol. 100, no. SPL CONTENT, pp. 1537–1550, 2012.

[2] J. P. De Campos Da Costa, W. B. Bastos, P. I. Da Costa, M. A. Zaghete, E. Longo, and J. P. Carmo, "Portable Laboratory Platform with Electrochemical Biosensors for Immunodiagnostic of Hepatitis C Virus," *IEEE Sens. J.*, vol. 19, no. 22, pp. 10701–10709, 2019.

[3] L. Wang, Q. Xiong, F. Xiao, and H. Duan, "2D nanomaterials based electrochemical biosensors for cancer diagnosis," *Biosens. Bioelectron.*, vol. 89, pp. 136–151, 2017.

[4] T. T. Tsai *et al.*, "Diagnosis of Tuberculosis Using Colorimetric Gold Nanoparticles on a Paper-Based Analytical Device," *ACS Sensors*, vol. 2, no. 9, pp. 1345–1354, 2017.

[5] S. J. Updike, M. C. Shults, B. J. Gilligan, and R. K. Rhodes, "A

subcutaneous glucose sensor with improved longevity, dynamic range, and stability of calibration," *Diabetes Care*, vol. 23, no. 2, pp. 208–214, 2000.

[6] C. W. Hanson and E. R. Thaler, "Electronic nose prediction of a clinical pneumonia score: Biosensors and microbes," *Anesthesiology*, vol. 102, no. 1, pp. 63–68, 2005.

[7] Y. H. Kim, S. Saini, D. Sahani, P. F. Hahn, P. R. Mueller, and Y. H. Auh, "Imaging diagnosis of cystic pancreatic lesions: Pseudocyst versus nonpseudocyst," *Radiographics*, vol. 25, no. 3, pp. 671–685, 2005.

[8] D. Dias and J. P. S. Cunha, "Wearable health devices—vital sign monitoring, systems and technologies," *Sensors (Switzerland)*, vol. 18, no. 8, 2018.

[9] Z. Zhang, H. Liu, and J. Deng, "A glucose biosensor based on immobilization of glucose oxidase in electropolymerized o-aminophenol film on platinized glassy carbon electrode," *Anal. Chem.*, vol. 68, no. 9, pp. 1632–1638, 1996.

[10] A. A. Saei, J. E. N. Dolatabadi, P. Najafi-Marandi, A. Abhari, and M. de la Guardia, "Electrochemical biosensors for glucose based on metal nanoparticles," *TrAC - Trends Anal. Chem.*, vol. 42, no. x, pp. 216–227, 2013.

[11] Y. Yu, J. Chen, and J. Zhou, "Parallel plate lab on a chip based on digital microuidics for on-chip electrochemical analysis," *J. Micromechanics Microengineering*, vol. 24, no. 1, 2014.

[12] O. S. Wolfbeis, M. Schäferling, and A. Dürkop, "Reversible Optical Sensor Membrane for Hydrogen Peroxide Using an Immobilized Fluorescent Probe, and its Application to a Glucose Biosensor," *Microchim. Acta*, vol. 143, no. 4, pp. 221–227, 2003.

[13] E. Scavetta, B. Ballarin, and D. Tonelli, "A cheap amperometric and optical sensor for glucose determination," *Electroanalysis*, vol. 22, no. 4, pp. 427–432, 2010.

[14] A. A. Essawy and M. S. Attia, "Novel application of pyronin y fluorophore as high sensitive optical sensor of glucose in human serum," *Talanta*, vol. 107, pp. 18–24, 2013.

[15] K. M. Quan, G. B. Christison, H. A. MacKenzie, and P. Hodgson, "Glucose determination by a pulsed photoacoustic technique: An experimental study using a gelatin-based tissue phantom," *Phys. Med. Biol.*, vol. 38, no. 12, pp. 1911–1922, 1993.

[16] R. Hu, A. C. Stevenson, and C. R. Lowe, "An acoustic glucose sensor," *Biosens. Bioelectron.*, vol. 35, no. 1, pp. 425–428, 2012.

[17] S. Kim *et al.*, "Noninvasive in vitro measurement of pig-blood d-glucose by using a microwave cavity sensor," *Diabetes Res. Clin. Pract.*, vol. 96, no. 3, pp. 379–384, 2012.

[18] S. Kim *et al.*, "In vitro monitoring of goat-blood glycemia with a microwave biosensor," *Curr. Appl. Phys.*, vol. 14, no. 4, pp. 563–569, 2014.

[19] I. L. Jernelv, K. Milenko, S. S. Fuglerud, D. R. Hjelme, R. Ellingsen, and A. Aksnes, "A review of optical methods for continuous glucose monitoring," *Appl. Spectrosc. Rev.*, vol. 54, no. 7, pp. 543–572, 2019.

[20] T. I. Valdes and F. Moussy, "In vitro and in vivo degradation of glucose oxidase enzyme used for an implantable glucose biosensor," *Diabetes Technol. Ther.*, vol. 2, no. 3, pp. 367–376, 2000.

[21] M. T. Novak, F. Yuan, and W. M. Reichert, "Modeling the relative impact of capsular tissue effects on implanted glucose sensor time lag and signal attenuation," *Anal. Bioanal. Chem.*, vol. 398, no. 4, pp. 1695–1705, 2010.

[22] N. M. M. Pires, T. Dong, U. Hanke, and N. Hoivik, "Recent developments in optical detection technologies in lab-on-a-chip devices for biosensing applications," *Sensors (Switzerland)*, vol. 14, no. 8, pp. 15458–15479, 2014.

[23] H. Jin *et al.*, "Flexible surface acoustic wave resonators built on disposable plastic film for electronics and lab-on-a-chip applications," *Sci. Rep.*, vol. 3, no. 2, pp. 1–8, 2013.

[24] D. J. Rowe, A. A. Abduljabar, A. Porch, D. A. Barrow, and C. J. Allender, "Improved Split-Ring Resonator for Micro fl uidic Sensing," vol. 62, no. 3, pp. 689–700, 2014.

[25] M. Hofmann, G. Fischer, R. Weigel, and D. Kissinger, "Microwave-based noninvasive concentration measurements for biomedical applications," *IEEE Trans. Microw. Theory Tech.*, vol. 61, no. 5, pp. 2195–2204, 2013.

[26] V. Turgul and I. Kale, "A novel pressure sensing circuit for non-invasive RF/microwave blood glucose sensors," *Mediterr. Microw. Symp.*, vol. 0, 2016.

[27] N. H. Cho *et al.*, "IDF Diabetes Atlas: Global estimates of diabetes prevalence for 2017 and projections for 2045," *Diabetes Res. Clin. Pract.*, vol. 138, pp. 271–281, 2018.

[28] L. Ekhlaspour *et al.*, "Comparative Accuracy of 17 Point-of-Care Glucose Meters," *J. Diabetes Sci. Technol.*, vol. 11, no. 3, pp. 558–566, 2017.

[29] J. H. Goh, A. Mason, A. I. Al-Shamma'a, M. Field, and P. Browning, "Lactate detection using microwave spectroscopy for in-situ medical applications," *Int. J. Smart Sens. Intell. Syst.*, vol. 4, no. 3, pp. 338–352, 2011.

[30] J. H. Goh, A. Mason, A. I. Al-Shamma'a, M. Field, M. Shackcloth, and P. Browning, "Non invasive microwave sensor for the detection of lactic acid in cerebrospinal fluid (CSF)," *J. Phys. Conf. Ser.*, vol. 307, no. 1, pp. 1–6, 2011.

[31] A. Mason, O. Korostynska, M. Ortoneda-Pedrola, A. Shaw, and A. Al-Shamma'A, "A resonant co-planar sensor at microwave frequencies for biomedical applications," *Sensors Actuators, A Phys.*, vol. 202, pp. 170–175, 2013.

[32] H. Sun, R. Li, G. Y. Tian, T. Tang, G. Du, and B. Wang, "Determination of complex permittivity of thin dielectric samples based on high-q microstrip resonance sensor," *Sensors Actuators, A Phys.*, vol. 296, pp. 31–37, 2019.

[33] A. Ebrahimi, J. Scott, and K. Ghorbani, "Differential sensors using microstrip lines loaded with two split-ring resonators," *IEEE Sens. J.*, vol. 18, no. 14, pp. 5786–5793, 2018.

[34] V. Turgul and I. Kale, "Characterization of the complex permittivity of glucose/water solutions for noninvasive RF/Microwave blood glucose sensing," *Conf. Rec. - IEEE Instrum. Meas. Technol. Conf.*, vol. 2016-July, no. 1, pp. 1–5, 2016.

[35] D. Mondal, N. K. Tiwari, and M. J. Akhtar, "Microwave Assisted Non-Invasive Microfluidic Biosensor for Monitoring Glucose Concentration," *Proc. IEEE Sensors*, vol. 2018-Octob, pp. 18–21, 2018.

[36] S. Harnsoongnoen and A. Wanthong, "Coplanar Waveguide Transmission Line Loaded with Electric-LC Resonator for Determination of Glucose Concentration Sensing," *IEEE Sens. J.*, vol. 17, no. 6, pp. 1635–1640, 2017.

[37] G. Govind and M. J. Akhtar, "Metamaterial-inspired microwave microfluidic sensor for glucose monitoring in aqueous solutions," *IEEE Sens. J.*, vol. 19, no. 24, pp. 11900–11907, 2019.

[38] A. Ebrahimi, W. Withayachumnankul, S. F. Al-Sarawi, and D. Abbott, "Microwave microfluidic sensor for determination of glucose concentration in water," *Mediterr. Microw. Symp.*, vol. 2015-Janua, pp. 1–3, 2015.

[39] Z. Abedeen and P. Agarwal, "Microwave sensing technique based label-free and real-time planar glucose analyzer fabricated on FR4," *Sensors Actuators, A Phys.*, vol. 279, pp. 132–139, 2018.

[40] R. Kumari and P. N. Patel, "A low-cost dielectric spectroscopic system using metamaterial open horn-ring resonator-inspired BSF and detection circuitry," *Appl. Phys. A Mater. Sci. Process.*, vol. 122, no. 7, pp. 1–10, 2016.

[41] R. Kumari, P. N. Patel, and R. Yadav, "An ENG resonator-based microwave sensor for the characterization of aqueous glucose," *J. Phys. D. Appl. Phys.*, vol. 51, no. 7, 2018.

[42] R. C. Lo, "Application of Microfluidics in Chemical

Engineering," 2013.

[43] L. Li and D. Uttamchandani, "A microwave dielectric biosensor based on suspended distributed MEMS transmission lines," *IEEE Sens. J.*, vol. 9, no. 12, pp. 1825–1830, 2009.

[44] J. A. Byford, K. Y. Park, and P. Chahal, "Metamaterial inspired periodic structure used for microfluidic sensing," *Proc. - Electron. Components Technol. Conf.*, vol. 2015-July, pp. 1997–2002, 2015.

[45] N. Sharafadinzadeh, M. Abdolrazzaghi, and M. Daneshmand, "Highly sensitive microwave split ring resonator sensor using gap extension for glucose sensing," *2017 IEEE MTT-S Int. Microw. Work. Ser. Adv. Mater. Process. RF THz Appl. IMWS-AMP 2017*, vol. 2018-Janua, no. September, pp. 1–3, 2018.

[46] C. G. Juan, E. Bronchalo, B. Potelon, C. Quendo, E. Ávila-Navarro, and J. M. Sabater-Navarro, "Concentration Measurement of Microliter-Volume Water-Glucose Solutions Using Q Factor of Microwave Sensors," *IEEE Trans. Instrum. Meas.*, vol. 68, no. 7, pp. 2621–2634, 2019.

[47] S. Harnsoongnoen and A. Wanthong, "Real-time monitoring of sucrose, sorbitol, D-glucose and D-fructose concentration by electromagnetic sensing," *Food Chem.*, vol. 232, pp. 566–570, 2017.

[48] T. Chretiennot, D. Dubuc, and K. Grenier, "Microwave-based microfluidic sensor for non-destructive and quantitative glucose monitoring in aqueous solution," *Sensors (Switzerland)*, vol. 16, no. 10, 2016.

[49] Y. Cui and P. Wang, "The design and operation of ultra-sensitive and tunable radio-frequency interferometers," *IEEE Trans. Microw. Theory Tech.*, vol. 62, no. 12, pp. 3172–3182, 2014.

[50] P. L. L. Bertarini, A. L. Sanches, and B. H. V. Borges, "Optimal code set selection and security issues in spectral phase-encoded time spreading (SPECTS) OCDMA systems," *J. Light. Technol.*, vol. 30, no. 12, pp. 1882–1890, 2012.

[51] H. ANSYS High Frequency Structure Simulator, "Ver. 15," *ANSYS Inc*.

[52] L. Liu, R. Pathak, L. J. Cheng, and T. Wang, "Real-time frequency-domain terahertz sensing and imaging of isopropyl alcohol-water mixtures on a microfluidic chip," *Sensors Actuators, B Chem.*, vol. 184, pp. 228–234, 2013.

[53] J. Kilpijärvi, N. Halonen, J. Juuti, and J. Hannu, "Microfluidic microwave sensor for detecting saline in biological range," *Sensors (Switzerland)*, vol. 19, no. 4, 2019.

[54] J. Bao *et al.*, "A 20-GHz Microwave Miniaturized Ring Resonator for nL Microfluidic Sensing Applications," *IEEE Sensors Lett.*, vol. 3, no. 6, pp. 1–4, 2019.

[55] X. Bao, I. Ocket, M. Zhang, J. Bao, D. Schreurs, and B. Nauwelaers, "Microwave Characterization of Liquid Mixtures with a Miniaturized Interdigital Sensor," *IMWS-AMP 2019 - 2019 IEEE MTT-S Int. Microw. Work. Ser. Adv. Mater. Process. RF THz Appl.*, pp. 157–159, 2019.